Austin Journal of Radiology

Open Access

Austin Publishing Group

Research Article

# Pulmonary Contrast- and Non-contrast- Enhanced Computed Tomography Image Registration Based on Multi-Resolution B-spline Transformation

**Jinxing Gao[1,2#]; Liyilei Su[1#]; Tiegong Wang[3#]; Yaozhou Chen[4]; Wenzhong Zhang[4]; Jing Li[5]; Chengwei Shao[4*]; Bingding Huang[1*]**

[1]College of Big Data and Internet, Shenzhen Technology University, China

[2]Wuerzburg Dynamics Inc., China

[3]Department of Radiology, Changhai Hospital, Naval Medical University (Second Military Medical University), China

[4]Guangdong Medical Devices Quality Surveillance and Test Institute, China

[5]Department of Pulmonary and Critical Care Medicine, Guangdong Provincial People's Hospital (Guangdong Academy of Medical Sciences), Southern Medical University, China

***Corresponding author: Bingding Huang**

College of Big Data and Internet, Shenzhen Technology University, China;

**Chengwei Shao,** Guangdong Medical Devices Quality Surveillance and Test Institute, China

Email: huangbingding@sztu.edu.cn; cwshao@sina.com

#These authors contributed equally to this article.

**Received:** September 05, 2023

**Accepted:** October 05, 2023

**Published:** October 12, 2023

## Abstract

Dynamic Contrast-Enhanced Computed Tomography (CE-CT) images play a vital role in clarifying lesion characteristics and surgical path planning for pulmonary interventional surgery. Lung deformations caused by respiration during scans make it difficult to accurately fuse CE-CT images into Non-Contrast-Enhanced Computed Tomography (NCE-CT) images. A precise image registration algorithm is a promising tool for handling problems related to aligning CE-CT images to NCE-CT images. In this study, we proposed a multi-resolution B-spline registration algorithm to register two-phase CE-CT (intra-arterial and intravenous) images into NCE-CT images. Initially, an in-house dataset with 10 pairs of lung computed tomography data (30 images during two phases of CE-CT and one phase of NCE-CT) was collected. Thereafter, we performed algorithmic optimization on this dataset and determined the optimal parameters for every step in the registration process. The Jacobian determinant of the transformation was used to reveal the rationality of the transformation. The registration results demonstrated that our algorithm reduced the target registration error to 0.59±0.51 mm. Three-dimensional lung reconstruction showed that the images were well aligned after registration upon observation. Moreover, the deformation pat-tern of local parenchymal tissue indicated that the transformation was reasonable. Our proposed method is a feasible and effective way of registering CE-CT and NCE-CT images. It can improve the accuracy and safety of surgical path planning and be applied in image-guided intervention methods, such as image-guided radiotherapy and computer-assisted surgical navigation.

**Keywords:** Contrast-Enhanced Computed Tomography (CE-CT); Non-Contrast-Enhanced Computed Tomography (NCE-CT); Image registration; B-spline

## Introduction

Dynamic Contrast-Enhanced Computed Tomography (CE-CT) images, including Intra-Arterial Contrast-Enhanced Computed Tomography (IA-CT) and intravenous contrast-enhanced computed tomography (IV-CT) images, accompanied with Non-Contrast-Enhanced Computed Tomography (NCE-CT) images have great potential in many clinical applications, such as clinical diagnosis, treatment planning, and image-guided interventions [1,2]. CE-CT involves acquiring a time sequence of images after contrast agent injection. Parametric images are then generated by fitting a pharmacokinetic model to its follow-up at each voxel, as the estimated parameters yield valuable information on healthy tissues and lesions [3]. The primary purpose of CE-CT is to further clarify lesion characteristics. More specifically, it is intended to clarify the relationship between occupying lesions and adjacent tissues and to better visualize the structures of the lungs and mediastinum. CE-CT can provide detailed anatomical structure information of the pulmonary vessels and lesions, while NCE-CT cannot.

With the development of image-guided navigation systems, the accuracy and efficiency of complex surgical interventions have been greatly improved [4]. In image-guided radiotherapy, CE-CT images are often fused with NCE-CT images and used for tumor target and critical structure delineation. However, patient motion, especially respiratory motion, may lead to an inaccurate fusion between CE-CT and NCE-CT images, reducing the




**Citation:** Gao J, Su L, Wang T, Chen Y, Zhang W, et al. Pulmonary Contrast- and Non-contrast-Enhanced Computed Tomography Image Registration Based on Multi-resolution B-spline Transformation. Austin J Radiol. 2023; 10(4): 1222.

treatment plan accuracy. In conventional image-guided interventional techniques, such as Computed Tomography (CT)-guided lung biopsies, patients are often asked to hold their breath for lung lesion localization in clinical practice. Repeated scanning cannot also be avoided, which can cause pain and increase radiation exposure. With the help of robot-assisted navigation systems, tracking devices, such as optical and electromagnetic tracking systems, can be used to track the patient anatomy in real time [5]. However, the relationship between the static guidance information and the moving anatomy remains unknown. Modeling the correlation of respiratory motion with the human surface then becomes a great challenge [6,7].

Image registration is a promising tool for handling problems related to aligning CE-CT images to NCE-CT images to resolve the motion effects. In medical imaging tasks, image registration aims to find a spatial correspondence between the points in the first and second image sets that has the exact patient-based coordinates or represents the same anatomic position [8]. In pulmonary lesion surgeries, data obtained from CE-CT images are often registered to data obtained from NCE-CT images to avoid the pulmonary vessels and to determine target points in the surgical path planning. The displacement field and the Jacobian determinant of the lung obtained from registration could thus be used for respiratory motion modeling. However, with existing techniques, the registration accuracy remains unsatisfactory. These techniques cannot meet the need during actual interventional surgery because of the asymmetric information between enhanced and non-enhanced images, including the gray distribution.

Some organs, such as the lung and heart, have internal aberrations due to autonomous movements during corresponding time intervals, making the images acquired at different times vary in characteristics. Currently, non-rigid registration is usually employed for these organs [9]. However, many challenges remain to be solved, such as local correspondence deficiency and large deformation of images, irregular physiological movement of the organ itself, and appearance of other factors during surgery.

B-spline [10] is a well-known approach for non-rigid image registration, since a change in a control point affects only the transformation within a local neighborhood of the point [11]. This method works by placing a uniformly spaced three-dimensional (3D) grid over the volume to be registered, with the lattice points acting as control points for tissue displacement. The displacement of each control point results in a deformation of the region surrounding the point in a way that makes the overall deformation as smooth as possible. B-spline has already shown potential for medical applications [12,13]. However, the grid size is difficult to determine and cannot be applied to all images. A coarse control grid allows for modeling global non-rigid deformations, while a fine control grid allows for modeling highly local deformations [14]. However, the registration is coarse with a large grid interval. Further, the global displacement is not extracted with a small grid interval, and it is easy to resort to a local optimal solution. Therefore, we employed a changing grid from coarse to fine for registration, which is suitable for most images.

Pulmonary image registration is challenging owing to the non-homogeneous soft tissues interlaced by the airways and vessels and the non-uniform intensity change during respiration. Therefore, we proposed an intensity-based non-rigid registration based on B-spline transformation with a coarse-to-fine strategy in this study. To our knowledge, existing intensity-based methods [15,16] are applied only between NCE-CT images and four-dimensional CT images in lung CT registration. No study has yet reported the application of pulmonary CE-CT image registration. Therefore, we applied our proposed algorithm to register pulmonary CE-CT (IA-CT and IV-CT) images to NCE-CT images.

**Our contributions in this work are summarized as follows:**

We employed B-spline transformation [17] for lung CT-to-CT (IA-CT, IV-CT, and NCE-CT) image registration and algorithmic optimization for a large displacement of lung data and determined the optimal parameters for every step in the registration process.

We presented a multi-resolution B-spline transformation method with changing grid intervals driven by commonly used intensity-based criteria for lung image registration. Images were smoothed and down-sampled to reduce complexity using a random sample and the B-spline-based interpolation algorithm, with Mutual Information (MI) as similarity measurements.

We generated the deformation field and the Jacobian determinant after registration, which could help model respiratory motions.

The experiments were conducted on our in-house dataset with 10 pairs of lung-enhanced CT data, reducing the Target Registration Error (TRE) to 0.59±0.51 mm. We also demonstrated image registration via observation based on 3D reconstruction. Furthermore, the Jacobian determinant of transformation was used to reveal the rationality of the transformation and the deformation pattern of local parenchymal tissue, which indicated that the transformation was reasonable. This method reduced the impact of lung deformation caused by respiratory movements on registration and could then be used in subsequent surgical navigation systems.

## Materials and Methods

### Dataset and Annotation

We collected lung CT data from 10 patients who underwent one phase of NCE-CT and two enhanced phases of CE-CT (IA-CT and IV-CT) at Changhai Hospital of Shanghai. Each CT image had a matrix size of 512×512 pixels in-plane and pixel spacing ranging from 0.654×0.654 mm to 0.912×0.912 mm. The number of slices varied from 320 to 395, and the slice thickness was 1 mm.

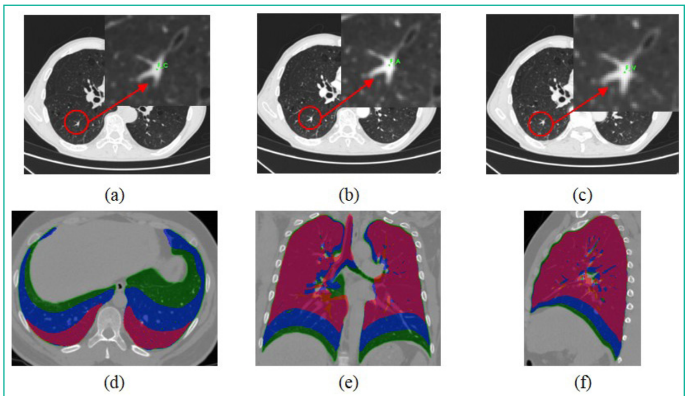


**Figure 1:** Axial slice of the NCE-CT and CE-CT images of case 1: (a) NCE-CT; the gray value of F_C is 7; (b) IA-CT; the gray value of F_A is 220; (c) IV-CT; the gray value of F_V is 143. Overlaying lung masks of case 9: (d) axial view; (e) coronal view; (f) sagittal view; with green masks representing the NCE-CT images, red masks representing the IA-CT images, and blue masks representing the IV-CT images.

The three CT images were obtained in the breath-holding state after respiration. Because of the two different enhancements, the intensity of the same feature point in the three images differed. Meanwhile, owing to the different respiration habits and control capabilities of patients, the three images of one patient may have different lung volumes corresponding to small or large deformations. Figure 1 shows the three CT images for case no. 1 and no. 9.

Generally, intra-subject CT images of the lung contain identifiable feature points, such as airway–tree and vascular–tree branch points. Herein, we randomly labeled 20 vascular feature points in each lobe of the lung (upper left, lower left, upper right, middle right, and lower right lungs) for each case under the guidance of specialized doctors. A total of 100 feature points were obtained. The corresponding feature points were found in the NCE-CT, IA-CT, and IV-CT images. To ensure annotation accuracy, we manually annotated all feature points. Figure 2 shows example feature points in the three CT images.

To verify the registration between the different CT images, we considered the NCE-CT images as the fixed images and the IA-CT and IV-CT images as the moving images. We studied the IA-CT images registered to the NCE-CT (N-A) images and the IV-CT images registered to the NCE-CT (N-V) images by comparing the B-spline registration displacements with the manually annotated feature point displacements (gold standard parameter). Supplementary Figure 1 shows the manually annotated displacements (Euclidean distance of the lung feature points) for all 10 cases. The pulmonary displacements varied from 1.54±0.89 mm (4-N-A) to 19.79±10.36 mm (9-N-A).

### Registration

The process of our proposed registration algorithm for the fixed and moving CT images is shown in Figure 3. The NCE-CT images were treated as the fixed images and the IA-CT and IV-CT images as the moving images. First, the fixed and moving images were smoothed and down-sampled to reduce complexity, defined as a Gaussian pyramid [26] (Figure 4). A sampler was used to sample the fixed image pixels for similarity measurement. Second, optimization was performed to calculate the transformation parameters. An interpolator was used for interpolating the moving image pixels for each transform iteration. Finally, we assessed the cost function or metrics to evaluate the registration quality.

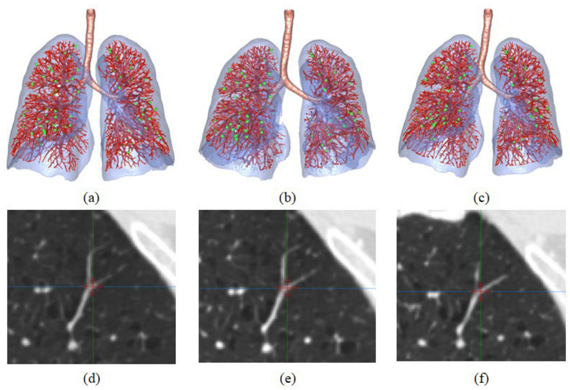


**Figure 2:** Distribution of the feature points (green points) selected on (a) NCE-CT; (b) IA-CT; and (c) IV-CT. The vessel trees are marked as red curves. The lung contours are colored blue. One example feature point (red cross) is highlighted at the vessel-tree branch on (d) NCE-CT, (e) IA-CT, and (f) IV-CT in the original images.

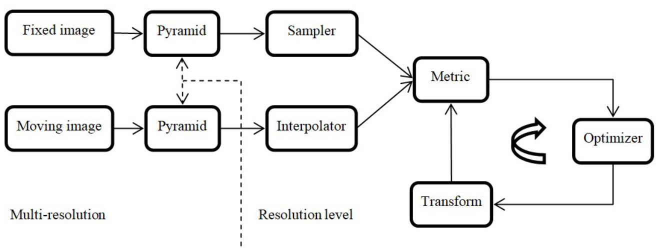


**Figure 3:** Process of the proposed registration algorithm for two CT images.

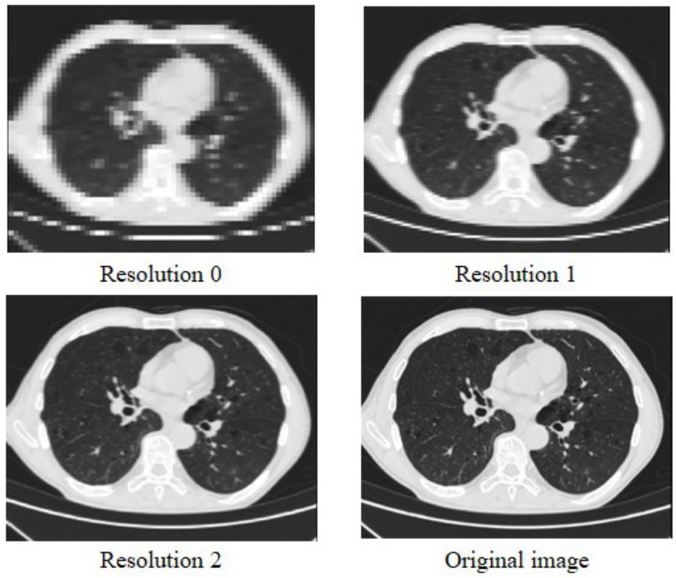


**Figure 4:** Multi-resolution strategy using a Gaussian pyramid (standard deviation $\sigma$=4, 2, and 1) and resampling spacing (8, 4, and 2 voxels, respectively).

Mathematically, the goal of the registration of a moving image to a fixed image is to find a displacement $\boldsymbol{h}(\boldsymbol{x})$ to form a transformation $\boldsymbol{T}_{\mu}(\boldsymbol{x}) = \boldsymbol{x} + \boldsymbol{h}(\boldsymbol{x})$ that makes $I_M(\boldsymbol{T}_{\mu}(\boldsymbol{x}))$ spatially aligned to $I_F(\boldsymbol{x})$. Herein, $\boldsymbol{\mu} = (\mu_1, \mu_2, \cdots)$ represents the vector of the transformation parameters. Registration is an optimization problem used to find the solution $\hat{\boldsymbol{\mu}}$ that minimizes $\mathcal{C}$:

$$\hat{\mu} = \arg\ \min_{\mu} \mathcal{C}(\mu; I_F, I_M) \qquad (1)$$

Where C is the cost function that measures the similarity of the fixed and deformed moving images. Since CE-CT and NCE-CT images are multi-modal images with different intensity distributions, MI [18] was employed as the similarity measurement. The optimization algorithm iteratively searched the optimal spatial transformation parameters based on the derivative of the measurement function.

Since the registration result is mainly determined by the image quality, lung deformation size, and registration parameters, three critical registration components were studied in our experiments, including sampling strategies, multi-resolution strategies, and similarity measurements. The experiments were conducted using the Elastix software, a toolbox for intensity-based medical image registration [29].

**The hyper-parameters used in the experiments were as follows:**

#### Sampling, Interpolation, and Optimization

Feature selection is the most critical step in the registration process. As we adopted intensity-based image registration, all voxels inside the lungs were extracted as feature spaces. We selected only the voxels in the feature space to compute the cost function and its derivative. Random sampling has been shown

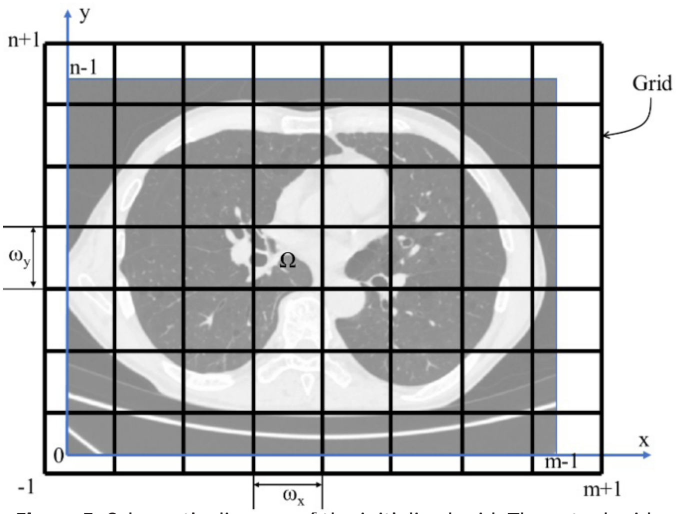


**Figure 5:** Schematic diagram of the initialized grid. The actual grid is three dimensional, and the grid at the z direction is the same as that at the x and y directions.

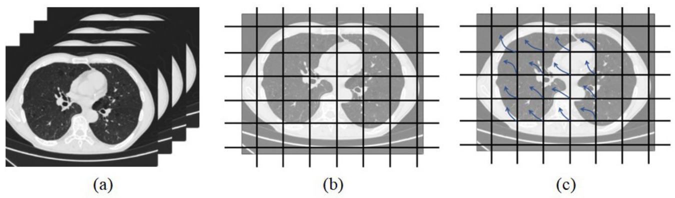


**Figure 6:** (a) Original images; (b) gird refinement; (c) control point movements.

to improve the smoothness of the cost function [19]; thus, we randomly selected a user-specified mask region from the fixed images.

Since each voxel in the CT image is represented by an integer, a feature voxel in the moving image may not be found in the fixed image. Interpolation is generally required to resolve this problem. Herein, we applied a B-spline-based interpolation algorithm [17], which provides a smoother interpolation by considering multiple points around the target point. The selection of the spline functions and the order of the selected spline functions determine the smoothness of the interpolated image grayscale and the amount of computation. The higher the order, the better the image quality, but with higher computational costs [20]. Considering both the smoothness and computation costs, we employed linear interpolation in the registration process and cubic B-spline interpolation for the image generation phase.

For optimization, we used an adaptive stochastic gradient descent, a more advanced version of the standard gradient descent with fewer parameters to set, which has been proven to be more robust [21].

**B-Spline Spatial Transformation with Multi-resolution Strategies**

The transformation model determines the deformations between the moving and fixed images. Herein, we employed B-spline transformation with multi-resolution strategies. B-splines are a linear combination of B-spline base curves and are calculated as follows [11]:

$$\boldsymbol{T}_{\mu}(\boldsymbol{x}) = \boldsymbol{x} + \sum_{x_k \in N_x} p_k \beta^3\left(\frac{x-x_k}{\omega}\right) \qquad (2)$$

where $\boldsymbol{x}_k$ is the control point; $\beta^3$ is the cubic multidimensional B-spline polynomial [20]; $p_k$ is the B-spline coefficient vector (control point displacement); $\omega$ is the B-spline control point interval; and $N_x$ is the set of all control points within the compact support of the B-spline at $\boldsymbol{x}$. B-spline transformation aims to refine the grid of registration images

$\Omega = \{(x, y, z) | 0 \le x \le m-1, 0 \le y \le n-1, 0 \le z \le l-1\}$ [23].

Specifically, an image is defined to be registered with resolution $m \times n \times l$ and a grid $\boldsymbol{\Phi}$ with $n_x \times n_y \times n_z$ control points at coordinates $\phi_{i,j,k}$ over the image area, as depicted in Fig. 5. The grid interval in the $x$, $y$, and $z$ directions is $\omega_x$ with $n_x$ control points, $\omega_y$ with $n_y$ control points, and $\omega_z$ with $n_z$ control points, respectively. Each control point has degrees of freedom in the three directions, so that the degrees of freedom for $\boldsymbol{\Phi}$ is $3 * n_x * n_y * n_z$ as follows:

$$\begin{cases} n_x = \left\lfloor \frac{m}{\omega_x} \right\rfloor + 3 \\ n_y = \left\lfloor \frac{n}{\omega_y} \right\rfloor + 3 \\ n_z = \left\lfloor \frac{l}{\omega_z} \right\rfloor + 3 \end{cases} \qquad (3)$$

Where $\lfloor \cdot \rfloor$ represents downward rounding. The number is added to 3 to the base of the downward rounding in the $x$, $y$, and $z$ directions to allow all regions, including the boundary points, in $\Omega$ to participate in the calculation of the spline fitting. It also satisfies the need for the subsequent calculation of the cubic B-spline transformation.

The B-spline transformation of any point $P = [x, y, z]^T$ on the moving image can be expressed as follows [24]:

$$\boldsymbol{T}(x, y, z) = \sum_{m=0}^{3} \sum_{n=0}^{3} \sum_{l=0}^{3} B_m(u) B_n(v) B_l(w) \phi_{i+m, j+n, k+l} \qquad (4)$$

with $i = \left\lfloor \frac{x}{\omega_x} \right\rfloor - 1$, $j = \left\lfloor \frac{y}{\omega_y} \right\rfloor - 1$, $k = \left\lfloor \frac{z}{\omega_z} \right\rfloor - 1$, $u = \frac{x}{\omega_x} - \left\lfloor \frac{x}{\omega_x} \right\rfloor$, $v = \frac{y}{\omega_y} - \left\lfloor \frac{y}{\omega_y} \right\rfloor$, $w = \frac{z}{\omega_z} - \left\lfloor \frac{z}{\omega_z} \right\rfloor$. $B_m(u)$

is the m-th cubic B-spline basis function [25]:

$$\begin{cases} B_0(u) = \frac{(1-u)^3}{6} \\ B_1(u) = \frac{3u^3 - 6u^2 + 4}{6} \\ B_2(u) = \frac{-3u^3 + 3u^2 + 3u + 1}{6} \\ B_3(u) = \frac{u^3}{6} \end{cases} \qquad (5)$$

The above-indicated equation acts as a weighting function, weighting the effect of each control point on $\boldsymbol{T}(x, y, z)$ by the distance from the control point to $(x, y, z)$. The displacement of each control point in each direction is solved via optimal searching. The B-spline basis function can easily simulate arbitrary nonlinear transformations and achieve good registration for images with arbitrary irregular deformations. As shown in Fig. 6, the movement of each control point finally formed a control grid with nonlinear deformation. The free deformation model is essentially a local control problem of local control by the cubic B-spline. In cases where in the grid spacing $\omega_x \times \omega_y \times \omega_z$ is determined, the transformed position of each point $(x, y, z)$ is determined only by the grid $\boldsymbol{\Phi}$. Simultaneously, any point of the image to be registered is affected only by the 4 × 4 control points in the nearby areas. The image to be registered will follow the grid deformation in the same manner and to the same extent by deforming the space formed by the control grid.

Therefore, the image resolution and grid interval of the B-spline determine the accuracy and efficiency of registration. When the grid interval is large, the efficiency is high with a low registration accuracy. In contrast, a small interval causes more flexible deformation but may generate unrealistic results and exhibit low efficiency. The fixed grid interval makes it difficult to balance the registration accuracy and efficiency. Moreover, in the actual image registration, it is unknown how large the grid interval should be set to obtain the most suitable result.

To overcome the limitation of fixed grid intervals, we applied the multi-resolution B-spline transformation method to balance accuracy and efficiency with changing grid intervals. In this strategy, hierarchical registration is used with the interval of the grid changing from large to small. The first layer uses a larger interval to simulate globally large deformations for coarse registration. The following layers use a gradually smaller grid interval to simulate locally small deformations for fine registration (Supplementary Figure 2).

### Evaluation Metrics

The evaluation of image registration accuracy is essential in quantifying the performance of registration algorithms. Owing to the lack of a gold standard method, multiple metrics are needed to evaluate the performance of registration algorithms. In our experiments, we assessed the registration results via TRE application, observation, and Jacobian determinant assessment [27]. The TRE was mainly utilized as a quantitative assessment to compare the performances of different registration models. It consists of identifying well-defined corresponding target points on registered images and measuring the 3D distance between them. In contrast, observation and Jacobian determinant assessment were conducted to assess the final optimal registration result.

The TRE was calculated as follows: 1) Manually annotate the feature point coordinates $\boldsymbol{p}_k$ in the fixed image and the corresponding feature point coordinates $\boldsymbol{q}_k$ in the moving image; 2) calculate the 3D displacement $\boldsymbol{h}(\boldsymbol{x})$ of the annotated feature points in the fixed image using the proposed registration algorithm; 3) calculate the feature point coordinates $\boldsymbol{T}(\boldsymbol{p}_k) = \boldsymbol{p}_k + \boldsymbol{h}(\boldsymbol{q}_k)$ after the displacement of the registration algorithm at $\boldsymbol{p}_k$; and 4) calculate the Euclidean distance between $\boldsymbol{q}_k$ and $\boldsymbol{T}(\boldsymbol{p}_k)$ as the TRE:

$$TRE = \|\boldsymbol{q}_k - \boldsymbol{T}(\boldsymbol{p}_k)\| \qquad (6)$$

With the observation method, we input the fixed and deformed moving images into visualization software to observe the degree of feature overlap. We then simultaneously performed 3D reconstruction of these images to monitor the degree of vascular overlap.

The Jacobian determinant [27] of the transformation field derived from image registration can be used to estimate local tissue deformation [28]. It estimates the pointwise expansion and contraction during deformations. The Jacobian determinant of the transformation $J(\boldsymbol{h}(\boldsymbol{x}))$ was calculated as follows:

$$J(\boldsymbol{h}(\boldsymbol{x})) = \begin{vmatrix} \frac{\partial h_1(\boldsymbol{x})}{\partial x_1} & \frac{\partial h_1(\boldsymbol{x})}{\partial x_2} & \frac{\partial h_1(\boldsymbol{x})}{\partial x_3} \\ \frac{\partial h_2(\boldsymbol{x})}{\partial x_1} & \frac{\partial h_2(\boldsymbol{x})}{\partial x_2} & \frac{\partial h_2(\boldsymbol{x})}{\partial x_3} \\ \frac{\partial h_3(\boldsymbol{x})}{\partial x_1} & \frac{\partial h_3(\boldsymbol{x})}{\partial x_2} & \frac{\partial h_3(\boldsymbol{x})}{\partial x_3} \end{vmatrix} \qquad (7)$$

Where $(h_1(\boldsymbol{x}), h_2(\boldsymbol{x}), h_2(\boldsymbol{x}))$ represents vectors in three dimensions of the deformation field at location $\boldsymbol{x}$. A Jacobian determinant of 1 indicates no volume change; >1, expansion; 0–1, shrinkage; and ≤0, folding. The quality of the displacement vector field can be quantified by indicating the fraction of foldings per image and determining the standard deviation of the Jacobian determinant.

## Results

### Sampling Strategies

Table 1 shows the TRE (mean±sd) among the 10 cases with and without a mask, corresponding to sample voxels from the entire images and inside the masks, respectively. Supplementary Table 1 shows that the registration effect greatly improved after limiting the sample voxels inside the mask, especially for case 9-N-A with the most considerable deformation.

### Multi-Resolution Strategies

The influence of the multi-resolution strategy was examined. Two critical components of the multi-resolution strategy were evaluated: final control point spacing and number of final control point resolution layers.

First, registration was performed using the final control point spacing: 64, 32, 16, or 8 mm. The results (Table 1 and Supplementary Table 2) showed that the performance improved from 64 mm to 16 mm. However, when the spacing was reduced to 8 mm, the accuracy had minimal improvements, and registration took longer. These results indicate that a final grid of 16 mm is sufficient for images with both small and large deformations, while a finer grid may result in unrealistic deformations and is more time consuming.

Second, registration was performed using the number of resolution layers: three, four, five, or six. The results (Table 1 and Supplementary Table 3) showed that the performance kept improving from three resolution layers to four resolution layers. However, when the number of resolution layers increased to five or six, the accuracy had almost no improvements, and a longer registration time was needed. These results indicate that the best number of resolution layers is four.

In conclusion, four resolution layers with a final grid interval of 16 mm is the best option for ensuring both accuracy and efficiency.

### Similarity Measurement

As mentioned above, we used MI as the cost function. The critical component of MI is the number of bins of the joint histogram; thus, we employed histogram bins of 8, 16, 32, or 64. As shown in Table 1 and Supplementary Table 4, the TRE continued to reduce with the number of histogram bins rising from 8 to 32. However, when the number of histogram bins reached 64, the performance started to decline. After overall consideration, the best number of histogram bins is 32.

### Final Results and Analysis

We calculated the TRE in all 10 cases with the manually annotated feature points. The results for each case are shown in Supplementary Fig. 3. We also present the displacement and TRE of case 9-N-A (with the most significant lung displacement) at each feature point in Supplementary Fig. 4. The mean TRE was 0.59±0.51 mm for all 10 cases. For the large-displacement

**Table 1:** Comparison of the TRE (millimeter) of the sampling strategies, multi-resolution strategies, and similarity measurements.

| | Mask | | Final control point spacing | | | | | Number of resolution layers | | | Histogram bins | | | |
|---|---|---|---|---|---|---|---|---|---|---|---|---|---|---|
| Before reg | Without | With | 64 | 32 | 16 | 8 | 3 | 4 | 5 | 6 | 8 | 16 | 32 | 64 |
| 5.52±5.46 | 1.22±2.51 | 0.59±0.55 | 0.88 ±0.82 | 0.68 ±0.59 | 0.59 ±0.55 | 0.59 ±0.61 | 0.79 ±2.16 | 0.59±0.51 | 0.59±0.50 | 0.59±0.55 | 1.06±2.08 | 0.72±0.98 | 0.59±0.51 | 0.75±1.95 |

**Table 2:** Jacobian determinant of each case in our dataset.

| Statistics | | Mean | Std | Minimum | Maximum | Folding |
|---|---|---|---|---|---|---|
| Case 1 | N-A | 1.01 | 0.04 | 0.89 | 1.18 | 0 |
| | N-V | 0.92 | 0.07 | 0.62 | 1.26 | 0 |
| Case 2 | N-A | 1.12 | 0.11 | 0.80 | 1.72 | 0 |
| | N-V | 1.12 | 0.10 | 0.79 | 1.65 | 0 |
| Case 3 | N-A | 1.00 | 0.12 | 0.73 | 1.83 | 0 |
| | N-V | 0.99 | 0.10 | 0.77 | 1.47 | 0 |
| Case 4 | N-A | 0.97 | 0.06 | 0.64 | 1.35 | 0 |
| | N-V | 1.01 | 0.05 | 0.83 | 1.30 | 0 |
| Case 5 | N-A | 1.01 | 0.03 | 0.83 | 1.26 | 0 |
| | N-V | 1.02 | 0.04 | 0.86 | 1.30 | 0 |
| Case 6 | N-A | 1.01 | 0.05 | 0.90 | 1.41 | 0 |
| | N-V | 0.92 | 0.06 | 0.65 | 1.39 | 0 |
| Case 7 | N-A | 1.03 | 0.05 | 0.91 | 1.69 | 0 |
| | N-V | 1.04 | 0.04 | 0.81 | 1.56 | 0 |
| Case 8 | N-A | 1.04 | 0.06 | 0.78 | 1.45 | 0 |
| | N-V | 1.11 | 0.08 | 0.83 | 1.55 | 0 |
| Case 9 | N-A | 0.69 | 0.14 | 0.29 | 1.45 | 0 |
| | N-V | 0.87 | 0.09 | 0.46 | 1.46 | 0 |
| Case 10 | N-A | 1.00 | 0.04 | 0.79 | 1.23 | 0 |
| | N-V | 0.96 | 0.05 | 0.67 | 1.28 | 0 |

images (case 9 with an average dis-placement of 20.0 mm), the TRE was 0.96±1.60 mm, indicating that the features in most lung regions were well matched, except for some individual feature points.

Using visualization software, we showed the 3D reconstruction overlapping of the blood vessels before and after registration (Supplementary Figure 5). Upon observation, the pulmonary vascular points were aligned well after the registration. The Jacobian determinant of all 10 cases is shown in Table 2 and Supplementary Figure 6. The Jacobian determinant in the remaining cases was around 1; this finding indicated that the lungs underwent different degrees of expansion and shrinkage, except for case 9-N-A, wherein most of the Jacobian determinant was <1 (substantial lung shrinkage). The absence of a Jacobian determinant of ≤0 in all 10 cases indicated that the transformation was reasonable.

## Conclusion

Pulmonary CE-CT is essential for clarifying lesions and vessels in the lungs. Similarly, registration of CE-CT and NCE-CT images is of great clinical importance, as it allows image fusion and evaluation of respiratory movements of the lungs. B-spline is a well-known approach for non-rigid image registration, but the grid size is difficult to determine and cannot be applied to all images. Therefore, we employed a changing grid from coarse to fine for the registration in our work. The main contribution of this study was that we attempted to apply our multi-resolution B-spline registration algorithm for CE-CT and NCE-CT images and to tune the parameters in the main components of registration to generate the best registration result. We also intended to generate the deformation field after registration, which could help model respiratory motions.

In our experiment, the registration algorithm was evaluated using CT images collected from Changhai Hospital of Shanghai. Twenty registrations of ten CT image pairs were performed, with the NCE-CT images set as the fixed images and the IA-CT and IV-CT images as the moving images. We applied multi-resolution B-spline transformation to align lung-enhanced CT images using lung contours and blood vessels as regions of interest, adaptive stochastic gradient decent as an optimizer, and linear as well as B-spline interpolation as interpolation algorithms. Furthermore, a Gaussian pyramid was used to smooth and down-sample the images in multi-resolution transformation.

We assessed the registration results based on the TRE, observations, and Jacobian determinant. The registration results demonstrated that our algorithm reduced the TRE to 0.59±0.51 mm. Upon observation with two-dimensional CT and 3D reconstruction, the feature points were found to be well aligned after registration. Furthermore, the Jacobian determinant of the transformation indicated that the transformation was reasonable. In general, our proposed method reduced the impact of lung deformation caused by respiratory movements on registration and could then be used in subsequent surgical navigation systems.

Considering the above-indicated analysis, we obtained good registration results. However, since our evaluation was based on only 10 cases, more CE-CT and NCE-CT data need to be collected and annotated to further evaluate the robustness of our algorithm. Regarding the shortage of extensive deformation data, our future research direction will focus on improving the accuracy of the registration algorithm for large-displacement and low-resolution images.

## Author Statements

### Acknowledgement

The authors would like to thank the colleagues who did the manual annotation.

### Funding Statement

This study was supported by the Project of the Educational Commission of Guangdong Province of China (No. 2022ZDJS113) and the School-Enterprise Cooperation Fund provided by Wuerzburg Dynamics Inc. to the Weiding Joint Laboratory of Medical Artificial Intelligence, Shenzhen Technology University.

### Author Contributions

Data curation, Yaozhou Chen; Formal analysis, JinXing Gao, Liyilei Su and Tiegong Wang; Funding acquisition, Bingding Huang; Methodology, JinXing Gao and Liyilei Su; Project administration, Chengwei Shao; Resources, Tiegong Wang, Wenzhong Zhang, Jing Li and Chengwei Shao; Supervision, Chengwei Shao and Bingding Huang; Validation, Yaozhou Chen and Wenzhong Zhang; Visualization, Jing Li; Writing – original draft, JinXing Gao and Liyilei Su; Writing – review & editing, Bingding Huang.

### Availability of Data and Materials

The CT data used to support the findings of this study are available from the corresponding author upon request.

### Ethics Approval

This work was a retrospective study, which was granted a waiver for ethical approval by the Ethics Committee of Changhai Hospital, Naval Medical University.

### Conflicts of Interest

The authors declare that they have no conflicts of interest to report regarding the present study.

### Supplementary Materials

The supplementary figures and tables of this article can be found in the separate supplementary files.

## References


1. Weir-Mccall JR, Joyce S, Clegg A, MacKay JW, Baxter G, Dendl LM, et al. Dynamic contrast–enhanced computed tomography for the diagnosis of solitary pulmonary nodules: a systematic review and meta-analysis. Eur Radiol. 2020; 30: 3310-23.

2. Li H, Bottani B, DeWees T, Low DA, Michalski JM, Mutic S et al. Prospective study evaluating the use of IV contrast on IMRT treatment planning for lung cancer. Med Phys. 2014; 41: 031708.

3. Kambadakone AR, Sahani DV. Body perfusion CT: technique, clinical applications, and advances. Radiol Clin North Am. 2009; 47: 161-78.

4. Anzidei M, Argirò R, Porfiri A, Boni F, Anile M, Zaccagna F, et al. Preliminary clinical experience with a dedicated interventional robotic system for CT-guided biopsies of lung lesions: a comparison with the conventional manual technique. Eur Radiol. 2015; 25: 1310-6.

5. Cleary K, Peters TM. Image-guided interventions: technology review and clinical applications. Annu Rev Biomed Eng. 2010; 12: 119-42.

6. Mcclelland JR, Hawkes DJ, Schaeffter T, King AP. Respiratory motion models: a review. Med Image Anal. 2013; 17: 19-42.

7. Büther F, Jones J, Seifert R, Stegger L, Schleyer P, Schäfers M. Clinical evaluation of a data-driven respiratory gating algorithm for whole-body PET with continuous bed motion. J Nucl Med. 2020; 61: 1520-7.

8. Haskins G, Kruger U, Yan P. Deep learning in medical image registration: A survey. Machine Vision and Applications. 2020; 31.

9. Rueckert D, Aljabar P. Nonrigid registration of medical images: theory, methods and applications. 2010; 27: 113-119.

10. de Boor CD. On calculating with B-splines. J Approx Theor. 1972; 6: 50-62.

11. Rueckert D, Sonoda LI, Hayes C, Hill DL, Leach MO, Hawkes DJ. Nonrigid registration using free-form deformations: application to breast MR images. IEEE Trans Med Imaging. 1999; 18: 712-21.

12. Sung, et al. Validation of deformable image registration by using a B-spline and optical-flow algorithm in head and neck cancer cases. Korean Physical Society. 2020; 76: 194-201.

13. Nair RR, Singh T. MAMIF: multimodal adaptive medical image fusion based on B-spline registration and non-subsampled shearlet transform. Multimedia Tool Appl. 2021; 80: 19079-105.

14. Yin Y, Hoffman EA, Lin CL. Mass preserving nonrigid registration of CT lung images using cubic B-spline. Med Phys. 2009; 36: 4213-22.

15. Xue P, Fu Y, Ji H, Cui W, Dong E. Lung respiratory motion estimation based on fast Kalman filtering and 4-D CT image registration. IEEE J Biomed Health Inform. 2021; 25: 2007-17.

16. Pennati F, Salito C, Aliverti A. Registration of lung CT images acquired in different respiratory ranges with 4DCT and HRCT. IEEE Publications. 2015; 2015: 2936-9.

17. Huizinga W, Klein S, Poot D. Fast multidimensional B-spline interpolation using template metaprogramming. Cham: Springer. 2014; 2014: 11-20.

18. Mattes D, Haynor DR, Vesselle H, Lewellen TK, Eubank W. PET-CT image registration in the chest using free-form deformations. IEEE Trans Med Imaging. 2003; 22: 120-8.

19. Thévenaz P, Bierlaire M, Unser M. Halton sampling for image registration based on mutual information. Sampling Theor Signal Image Process. 2008; 7: 141-71.

20. Unser M, M. Splines: a perfect fit for signal and image processing. IEEE Signal Process Mag. 2002; 16: 22-38.

21. Klein S, Pluim JPW, Staring M, Viergever MA. Adaptive stochastic gradient descent optimisation for image registration. Int J Comput Vis. 2009; 81: 227-39.

22. Sinha NK, Griscik MP. A stochastic approximation method. IEEE Trans Syst Man Cybern. 2007; 1: 338-44.

23. Pluim JPW, Maintz JB, Viergever MA. Image registration by maximization of combined mutual information and gradient information. IEEE Trans Med Imaging. 2000; 19: 809-14.

24. Tustison NJ, Avants BA, Gee JC. Improved FFD B-spline image registration. 2007 IEEE 11th International Conference on Computer Vision. IEEE Publications. 2007.

25. Xie Z, Farin GE. Image registration using hierarchical B-splines. IEEE Trans Vis Comput Graph. 2004; 10: 85-94.

26. Mo H, Maoyun Yang, Xiaobin Li, Jinwei Xia, Nana Wang, Xiaolin Wang, et al. Research on new nano-material based US-MRI registration. In: IEEE advanced information management, communicates, electronic and automation control conference (IMCEC). 2016; 2016: 1408-11.

27. Cao K, Ding K, Reinhardt JM, Christensen GE. Improving intensity-based lung CT registration accuracy utilizing vascular information. Int J Biomed Imaging. 2012; 2012: 285136.

28. Reinhardt JM, Ding K, Cao K, Christensen GE, Hoffman EA, Bodas SV. Registration-based estimates of local lung tissue expansion compared to xenon CT measures of specific ventilation. Med Image Anal. 2008; 12: 752-63.

29. Klein S, Staring M, Murphy K, Viergever MA, Pluim JP. elastix: A Toolbox for Intensity-Based Medical Image Registration. IEEE Trans Med Imaging. 2010; 29: 196-205.